



# Atomic-level insights into the steric hindrance effect of single-atom Pd catalyst to boost the synthesis of dimethyl carbonate

Shufang Ji<sup>a</sup>, Yuanjun Chen<sup>a</sup>, Guofeng Zhao<sup>b,\*</sup>, Yu Wang<sup>c</sup>, Wenming Sun<sup>d,\*</sup>, Zedong Zhang<sup>a</sup>, Yong Lu<sup>b</sup>, Dingsheng Wang<sup>a,\*</sup>

<sup>a</sup> Department of Chemistry, Tsinghua University, Beijing 100084 China

<sup>b</sup> School of Chemistry and Molecular Engineering, Shanghai Key Laboratory of Green Chemistry and Chemical Processes, East China Normal University, Shanghai 200062, China

<sup>c</sup> Shanghai Synchrotron Radiation Facility, Shanghai Advanced Research Institute, Chinese Academy of Sciences, Shanghai 201204, China

<sup>d</sup> College of Science, China Agricultural University, Beijing 100193, China

## ARTICLE INFO

### Keywords:

Single-atom catalysts  
Palladium  
Atom spatial confinement  
Dimethyl carbonate

## ABSTRACT

Atomic-level insight into the unique catalytic capability of single-atom catalysts that distinguished from nanometer-sized counterparts is highly desirable for catalyst design and catalysis research. By synthesizing single Pd atoms supported on TiO<sub>2</sub> as a catalyst, here we demonstrate a steric hindrance effect of single atoms induced by the unique isolation of single-atom active sites to achieve a remarkable enhancement on catalytic performance in the synthesis of dimethyl carbonate. Experimental results and density functional theory calculations reveal that such steric hindrance effect of single atoms favors the yield of the desired product dimethyl carbonate against further reacting with intermediates to form byproduct, because no extra Pd species around single Pd atoms provide active sites to further adsorb and activate substrates directly. The discovery of such steric hindrance effect is a valuable supplement to single-atom catalysis, and may promote single-atom catalysts to be widely applied in selective catalytic reactions.

## 1. Introduction

Single-atom catalysts (SACs) with maximum atom-utilization efficiency and unique properties are emerging as a new frontier in catalysis. [1–11] Featured with unsaturated coordination environment and uniform structural configuration of metal active centers as well as strong metal-support interaction, SACs have delivered excellent catalytic performance in various reactions. [12–23] Distinguished from conventional nanocatalysts, [24] SACs do not exist metal-metal bonds and generally carry partially positive charges. [25–27] The spatial atomic isolation and unique electronic structure endow SACs with particular adsorption and activation modes of substrates compared with traditional nanoparticles, thereby, leading to different catalytic reaction pathways catalyzed by SACs. [28–37] Although some advanced works have reported that SACs exhibited unexpected catalytic capability that nanometer-sized counterparts do not possess, more efforts should be paid to atomic-level insight into the catalytic specificity of SACs.

As an important and environmentally friendly organic compound, dimethyl carbonate (DMC) has attracted extensive attention because of

its excellent physicochemical properties and widespread application in the industrial field. [38–40] DMC can be used as building blocks to replace toxic and carcinogenic compounds to achieve green synthesis of various organic chemicals. [41,42] Given high dielectric constant, DMC is regarded as a superior electrolyte solvent in lithium ion batteries. [43] Additionally, owing to high oxygen content, favorable gasoline/water partition coefficient and low toxicity, DMC can serve as a promising fuel additive to reduce engine emissions and promote combustion. [44–46] Among many synthetic approaches for DMC, vapor-phase methyl nitrite (MN) carbonylation ( $\text{MN} + \text{CO} \rightarrow \text{DMC} + \text{NO}$ ) is considered as the most promising new-generation route. [47] Numerous efforts have been made in Pd-based nanomaterials to catalyze the synthesis of DMC via this route, however, the performance of these nanocatalysts is still far away from satisfactory, especially, the side reaction for the formation of byproduct dimethyl oxalate (DMO) is hard to be limited. [48,49] Inspired by structural specificity of SACs, employing single-atom Pd catalysts for the catalytic synthesis of DMC is expected to improve catalytic performance, but it still remains unexplored.

Herein, we demonstrate a steric hindrance effect of single atoms to

\* Corresponding authors.

E-mail addresses: [gzhao@chem.ecnu.edu.cn](mailto:gzhao@chem.ecnu.edu.cn) (G. Zhao), [swm@mail.sdu.edu.cn](mailto:swm@mail.sdu.edu.cn) (W. Sun), [wangdingsheng@mail.tsinghua.edu.cn](mailto:wangdingsheng@mail.tsinghua.edu.cn) (D. Wang).

<https://doi.org/10.1016/j.apcatb.2021.120922>

Received 22 August 2021; Received in revised form 7 November 2021; Accepted 9 November 2021

Available online 18 November 2021

0926-3373/© 2021 Elsevier B.V. All rights reserved.

enhance catalytic activity and selectivity. Such steric hindrance effect derives from the isolation of single-atom active sites. In this work, a single-atom Pd catalyst with isolated Pd atoms anchored on the anatase TiO<sub>2</sub> (SA-Pd<sub>1</sub>/TiO<sub>2</sub>) is synthesized and employed to reveal this steric hindrance effect. In the synthesis of DMC, the SA-Pd<sub>1</sub>/TiO<sub>2</sub> catalyst exhibits higher activity and selectivity compared with nanometer-sized Pd counterparts. The experimental results and density functional theory (DFT) calculations elucidate that this steric hindrance effect of single atoms helps to prevent the desired product DMC from further reacting with intermediates to form byproduct DMO, because no extra Pd species around single Pd atoms can offer active sites to dissociate substrate MN and supply new OCH<sub>3</sub> radical to initiate the DMO formation reaction. The discovery of such steric hindrance effect not only extends our understanding of unique catalytic behaviour of SACs, but also promotes SACs to be widely applied in selective catalytic reactions.

## 2. Experimental Section

### 2.1. Chemicals

Tetraammine dichloropalladium (II) monohydrate (Pd(NH<sub>3</sub>)<sub>4</sub>Cl<sub>2</sub>·H<sub>2</sub>O, 99.9%) and sodium tetrachloropalladate(II) (Na<sub>2</sub>PdCl<sub>4</sub>, 99.9%) were purchased from Alfa Aesar. Titanium oxide (TiO<sub>2</sub>, 99.8%, 5–10 nm) and poly (N-vinyl-2-pyrrolidone) (PVP, MW=30000) were purchased from Aladdin. Sodium hydroxide (NaOH), hydrochloric acid (HCl, 37%), potassium iodide and formamide (FA) were purchased from the Beijing Chemical Reagents, P.R. China. All of the reagents were analytical grade and were used without further purification.

### 2.2. Synthesis of Na<sub>x</sub>H<sub>2-x</sub>Ti<sub>3</sub>O<sub>7</sub> nanotubes

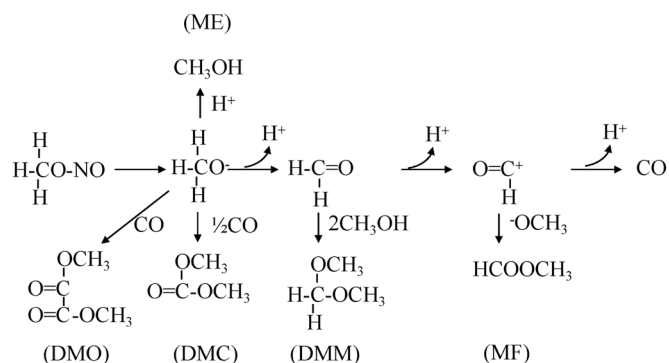
In a typical synthesis process of the titanate nanotubes (Na<sub>x</sub>H<sub>2-x</sub>Ti<sub>3</sub>O<sub>7</sub>), [50] 1 g of TiO<sub>2</sub> and an aqueous solution of NaOH (10 M, 30 mL) were added into a 50 mL Teflon-lined stainless-steel autoclave, stirred to form a suspension and then hydrothermally treated at 130 °C for 3 days. When the reaction is finished, the as-obtained precipitate was separated, washed with deionized water for several times and finally dried at 60 °C for 12 h.

### 2.3. Synthesis of SA-Pd<sub>1</sub>/TiO<sub>2</sub> and Pd-free TiO<sub>2</sub>

In a typical synthesis process of SA-Pd<sub>1</sub>/TiO<sub>2</sub>, Pd(NH<sub>3</sub>)<sub>4</sub>Cl<sub>2</sub>·H<sub>2</sub>O (1.5 mg) was dissolved in an aqueous solution of HCl (0.1 M, 20 mL) to form a clarified solution. The as-prepared titanate nanotubes (0.2 g) were added into the above solution and ultrasonic treatment for 30 min. The resulting mixture subsequently was stirred for 24 h at room temperature. The precipitate was separated, washed with deionized water and then dried under vacuum at 60 °C for 12 h. The as-prepared powder was collected and calcined in a muffle furnace at 400 °C for 1 h, then transferred into a tube furnace at 200 °C for 1 h under the 5% H<sub>2</sub>/Ar atmosphere with a heating rate of 2 °C min<sup>-1</sup>. The content of Pd was measured to be 0.12 wt% by inductively coupled plasma atomic emission spectroscopy (ICP-AES). Pd-free TiO<sub>2</sub> nanotubes were prepared with the same synthesis procedure of SA-Pd<sub>1</sub>/TiO<sub>2</sub> except Pd(NH<sub>3</sub>)<sub>4</sub>Cl<sub>2</sub>·H<sub>2</sub>O was not added.

### 2.4. Synthesis of nano-Pd/TiO<sub>2</sub>

In a typical synthesis process of palladium nanoparticles, [51] PVP (50 mg), KI (17 mg), FA (5 mL) were mixed in a 50 mL mouth flask and stirred to form homogenous solution. When the reaction solution was heated at 120 °C, the Na<sub>2</sub>PdCl<sub>4</sub> (30 mg) were quickly added into it and kept 120 °C for 10 min. The resulting Pd nanoparticles were precipitated by acetone, collected by centrifugation and dispersed in 10 mL of methanol. The Pd nanoparticles dispersion (2 mL) and 200 mg as-prepared Pd-free TiO<sub>2</sub> subsequently were dispersed in 20 mL



Scheme 1. The pathway network for the reaction of CO and MN.

methanol with stirring for 6 h. The product marked as nano-Pd/TiO<sub>2</sub> was precipitated by centrifugation and dried at 60 °C for 8 h. The content of Pd was measured to be 1.05 wt% by ICP-AES.

### 2.5. Characterizations

Morphologies and sizes of samples were determined by using a Hitachi H-800 TEM operated at 100 kV. Crystalline natures of samples were measured by a Rigaku RU-200b X-ray powder diffractometer (XRD) with Cu K $\alpha$  radiation ( $\lambda = 1.5406 \text{ \AA}$ ). The high-resolution characterization, atomic spatial resolution characterization and the elemental mappings of samples were collected on a Titan 80–300 STEM equipped with cold emitter and a probe aberration-corrected microscope, operated at 300 kV. XPS experiments were performed on a ULVAC PHI Quantera microprobe. The Pd concentrations of samples were measured by the inductively coupled plasma atomic emission spectroscopy (ICP-AES). The zeta potential was obtained by using HORIBA SZ-100 under room temperature. The GC analysis was determined using a Thermo Trace 1300 series GC with a FID detector using a capillary column (TR-5MS, from Thermo Scientific, length 30 m, i.d. 0.25 mm, film 0.25  $\mu\text{m}$ ). The X-ray absorption fine structure (XAFS) spectra data of samples at Pd K-edge were collected at BL14W1 station in Shanghai Synchrotron Radiation Facility (SSRF), operated at 3.5 GeV with a maximum current of 250 mA. The XAFS data of SA-Pd<sub>1</sub>/TiO<sub>2</sub> catalyst was collected at room temperature in fluorescence excitation mode using a Lytle detector and the references (Pd foil and PdO) were recorded in transmission mode using ionization chamber.

### 2.6. Catalytic testing

The catalyst testing for MN carbonylation to DMC was carried out in a fixed-bed quartz tube reactor (500 mm length by 10 mm inner diameter) with feed gas containing containing 11.5 vol% MN, 8.0 vol% CO and a balance of 80.5 vol% N<sub>2</sub> (molar ratio of MN/CO/N<sub>2</sub> = 1/0.7/7) with a weight hourly space velocity (WHSV) of 18000 L·kg<sub>cat</sub><sup>-1</sup>·h<sup>-1</sup> (based on catalyst weight) and a gas hourly space velocity (GHSV) of 25000 h<sup>-1</sup> (based on catalyst volume). The N<sub>2</sub>, CO and MN were all controlled by three calibrated mass flow controllers, and the flow rate was 60 mL/min. The 200 mg catalysts, including SA-Pd<sub>1</sub>/TiO<sub>2</sub>, nano-Pd/TiO<sub>2</sub> and Pd-free TiO<sub>2</sub>, were respectively packed into the quartz tubular reactor while a thermocouple was placed in the middle of the catalyst bed for monitoring its temperature. The compositions of the feed gas and product components were analyzed by using an online gas chromatograph (GC) equipped with a flame ionization detector (FID) connected to an Innovax PEG-20 M capillary column (HP) and a TCD connected to a ShinCarbon ST packed column (DIKMA). In this process, the pathway network for the reaction of CO and MN was shown in Scheme 1:

The Pd-catalyzed carbonylation of MN to DMC mainly includes four reactions, and accordingly, the MN conversion and product selectivity based on MN were calculated as following:

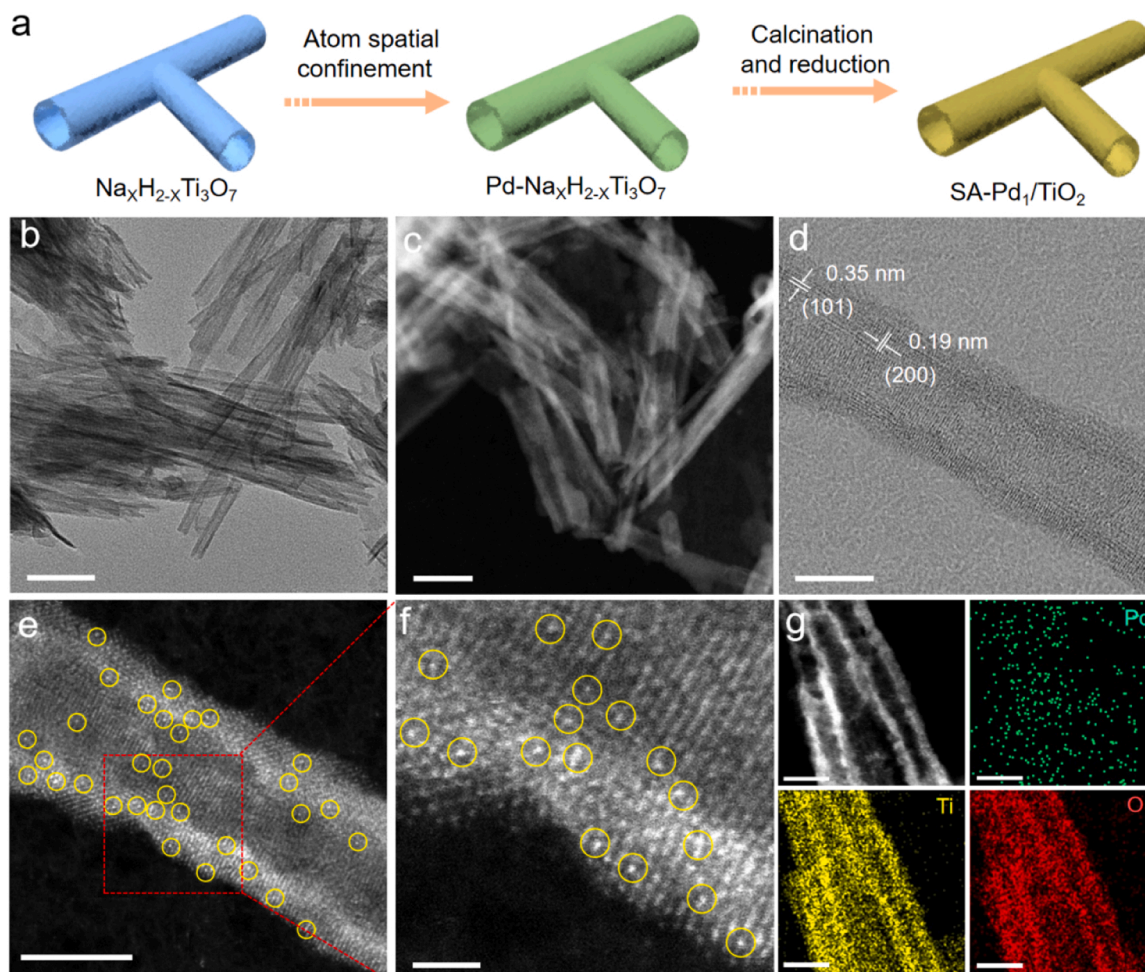


**Fig. 1.** Structural characterization of SA-Pd<sub>1</sub>/TiO<sub>2</sub> catalyst. (a) Illustration of preparation process of the SA-Pd<sub>1</sub>/TiO<sub>2</sub> catalyst. (b) TEM image, (c) HAADF-STEM image, (d) HRTEM image and the lattice fringe for SA-Pd<sub>1</sub>/TiO<sub>2</sub> catalyst. Scale bar, 50 nm in b; 20 nm in c; 5 nm in d. (e) Aberration-corrected HAADF-STEM image and (f) the corresponding enlarged image of SA-Pd<sub>1</sub>/TiO<sub>2</sub> catalyst. Scale bar, 5 nm in e; 1 nm in f; (g) HAADF-STEM image and the corresponding element maps showing distributions of Pd (green), Ti (yellow), O (red), respectively. Scale bar, 10 nm in g.

$$\text{MNConversion} = \frac{2 * n_{\text{DMO}} + 2 * n_{\text{DMC}} + n_{\text{ME}} + (4/3 * (n_{\text{MF}} - 1/2 * n_{\text{ME}}) + n_{\text{ME}})}{n_{\text{MN}} + 2 * n_{\text{DMO}} + 2 * n_{\text{DMC}} + n_{\text{ME}} + (4/3 * (n_{\text{MF}} - 1/2 * n_{\text{ME}}) + n_{\text{ME}})} * 100\%$$

$$\text{DMCSelectivity} = \frac{2 * n_{\text{DMC}}}{2 * n_{\text{DMO}} + 2 * n_{\text{DMC}} + n_{\text{ME}} + (4/3 * (n_{\text{MF}} - 1/2 * n_{\text{ME}}) + n_{\text{ME}})} * 100\%$$

$$\text{DMOSelectivity} = \frac{2 * n_{\text{DMO}}}{2 * n_{\text{DMO}} + 2 * n_{\text{DMC}} + n_{\text{ME}} + (4/3 * (n_{\text{MF}} - 1/2 * n_{\text{ME}}) + n_{\text{ME}})} * 100\%$$

$$\text{MESelectivity} = \frac{n_{\text{ME}}}{2 * n_{\text{DMO}} + 2 * n_{\text{DMC}} + n_{\text{ME}} + (4/3 * (n_{\text{MF}} - 1/2 * n_{\text{ME}}) + n_{\text{ME}})} * 100\%$$

$$\text{MFSelectivity} = \frac{4/3 * (n_{\text{MF}} - 1/2 * n_{\text{ME}}) + n_{\text{ME}}}{2 * n_{\text{DMO}} + 2 * n_{\text{DMC}} + n_{\text{ME}} + (4/3 * (n_{\text{MF}} - 1/2 * n_{\text{ME}}) + n_{\text{ME}})} * 100\%$$

Where  $n_i$  denotes the molar amount of feed gas or product  $i$ . ME is an abbreviation for methanol.

The space-time yield (STY) of DMC, the weight-time yields (WTY) of DMC and turnover frequencies (TOFs) were calculated using a reported method. [52].

The space time yield (STY) of DMC was calculated as follows:

$$\text{STY}_{\text{DMC}} = \frac{m_{\text{DMC}}}{L_{\text{cat}} \times t}$$

The weight-time yields (WTY) of DMC were calculated as follows:

$$\text{WTY}_{\text{DMC}} = \frac{m_{\text{DMC}}}{m_{\text{cat}} \times t}$$

The turnover frequencies (TOFs) of DMC was calculated as follows:

$$\text{TOF}_{\text{DMC}} = \frac{n_{\text{DMC}}}{n(\text{Pd})_{\text{cat}} \times t}$$

The turnover frequencies (TOFs) of MN was calculated as follows:

$$\text{TOF}_{\text{MN}} = \frac{n_{\text{MN}}}{n(\text{Pd})_{\text{cat}} \times t}$$

$m_{\text{DMC}}$ : the mass of DMC (g);  $L_{\text{cat}}$ : the volume of catalysts (L);  $t$ : reaction time (h);  $n_{\text{DMC}}$ : the moles of produced DMC (mol);  $n_{\text{MN}}$ : the moles of converted MN (mol);  $n(\text{Pd})_{\text{cat}}$ : the molar of efficient palladium (mol). To compare utilization efficiency of each Pd atom, the total amounts of active Pd sites were measured by ICP-AES.



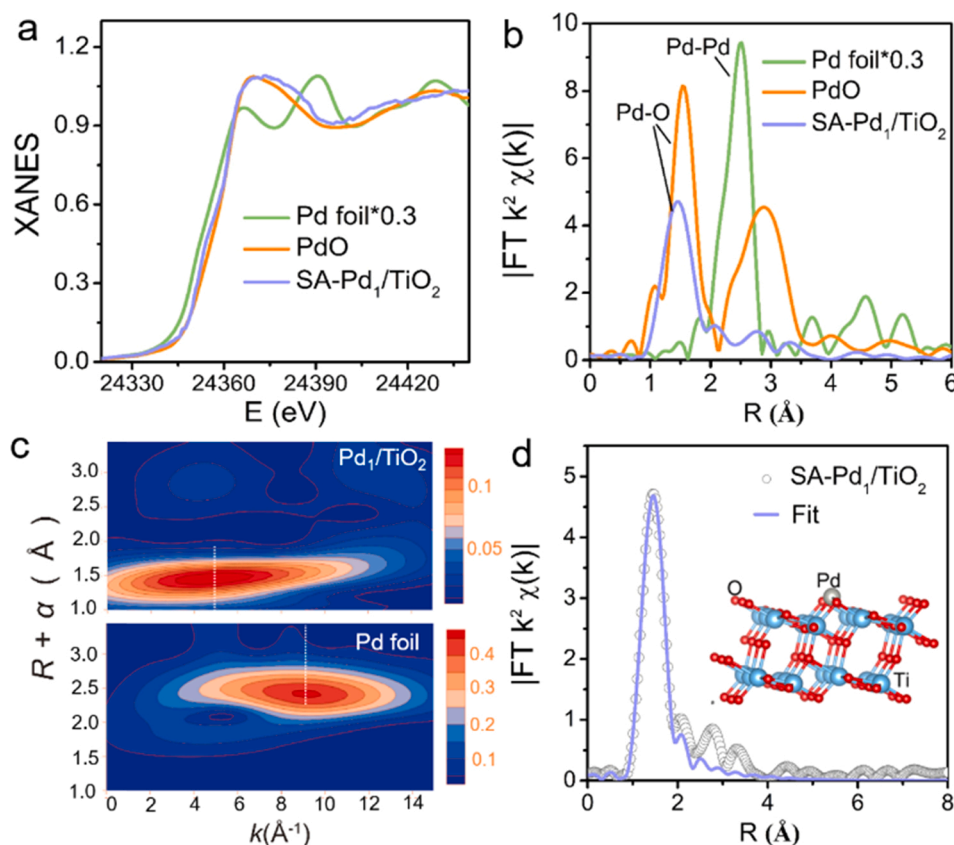


**Fig. 2.** Atomic structural analysis of SA-Pd<sub>1</sub>/TiO<sub>2</sub> catalyst. (a) XANES spectra and (b) EXAFS Fourier transformed (FT)  $k^2$ -weighted  $\chi(k)$  function spectra of SA-Pd<sub>1</sub>/TiO<sub>2</sub>, Pd foil and PdO. (c) WT of SA-Pd<sub>1</sub>/TiO<sub>2</sub>. The color in the contour figure indicates the moduli of the Morlet wavelet transform. (d) Fit spectra of SA-Pd<sub>1</sub>/TiO<sub>2</sub>. Inset: the structural model of Pd<sub>1</sub>/TiO<sub>2</sub>.

## 2.7. Computational method

Spin-polarized DFT calculations were carried out using the CASTEP [53,54] package with ultrasoft pseudopotentials and PBE[55] generalized gradient approach. The energy cutoff of 380 eV was used for the plane-wave basis set. The constructed TiO<sub>2</sub>(101) surface contains 24 Ti atoms and 48 O atoms. The top six atomic layers were relaxed fully while the other atomic layers were frozen during the geometry optimization. The Brillouin zone was sampled with  $1 \times 1 \times 1$  (for bulk TiO<sub>2</sub>, set as  $4 \times 4 \times 2$ ). The convergence thresholds between optimization cycles for energy change and maximum force were set as  $10^{-5}$  eV/atom and 0.03 eV/Å. The transition states were searched by the generalized synchronous transit (LST/QST) method.[56] The algorithm performs a linear synchronous transit (LST) optimization, followed by repeated conjugate gradient minimizations and quadratic synchronous transit (QST) maximizations until a transition state has been located.

## 3. Results and Discussion

### 3.1. Catalyst synthesis and characterization

We utilize atom spatial confinement (ASC) strategy to prepare single-atom Pd supported on anatase TiO<sub>2</sub> (SA-Pd<sub>1</sub>/TiO<sub>2</sub>) catalyst (Fig. 1a). Firstly, the titanate Na<sub>x</sub>H<sub>2-x</sub>Ti<sub>3</sub>O<sub>7</sub> ( $x = 0.75$ ) nanotubes with multilayered tubular structure were synthesized as raw materials (Fig. S1). Then, the titanate nanotubes were mixed with the Pd(NH<sub>3</sub>)<sub>4</sub><sup>2+</sup> complex. In this procedure, due to electrostatic interaction with a negatively charged two-dimensional (2D) TiO<sub>3</sub><sup>2-</sup> layers (Fig. S2), the Pd(NH<sub>3</sub>)<sub>4</sub><sup>2+</sup> was attracted into interlayer space of titanate and achieved intercalation through ion exchange with interlayer host ion Na<sup>+</sup>, leading to confinement of Pd complex in the 2D interlayer space of titanate. Upon the

subsequent calcination, the Pd-intercalated titanate (Pd-Na<sub>x</sub>H<sub>2-x</sub>Ti<sub>3</sub>O<sub>7</sub>) underwent phase transformation into anatase TiO<sub>2</sub>, finally forming the SA-Pd<sub>1</sub>/TiO<sub>2</sub>-C, as confirmed by XRD peaks indexed to anatase TiO<sub>2</sub> (Fig. S3). Finally, after reduction, the SA-Pd<sub>1</sub>/TiO<sub>2</sub> catalyst was formed. The evolutionary trajectory of SA-Pd<sub>1</sub>/TiO<sub>2</sub> was traced by X-ray powder diffraction (XRD) patterns (Fig. S3).

Transmission electron microscopy (TEM) image (Fig. 1b) and high-angle annular dark-field scanning TEM (HAADF-STEM) image (Fig. 1c) demonstrate that SA-Pd<sub>1</sub>/TiO<sub>2</sub> retains the uniform tubular morphology. As shown in Fig. 1d, high-resolution TEM (HRTEM) images of SA-Pd<sub>1</sub>/TiO<sub>2</sub> shows that the lattice spacings are about 0.19 nm and 0.35 nm, which indicate the (200) plane and (101) plane on the TiO<sub>2</sub> surface in SA-Pd<sub>1</sub>/TiO<sub>2</sub> and no metal Pd nanoparticles are observed on TiO<sub>2</sub> nanotube surface. Furthermore, aberration-corrected HAADF-STEM (AC HAADF-STEM) was employed. As shown in Figs. 1e and 1f, some isolated bright dots highlighted by yellow circles can be clearly distinguished, which are identified as Pd atoms. Energy-dispersive X-ray spectroscopy (EDS) analysis of SA-Pd/TiO<sub>2</sub> demonstrates that Pd, Ti and O are homogeneously dispersed (Fig. 1g). The content of Pd is measured to be 0.12 wt% by inductively coupled plasma atomic emission spectroscopy (ICP-AES). The Pd XPS spectra of SA-Pd<sub>1</sub>/TiO<sub>2</sub> catalyst are shown in the Fig. S4. The peaks at the binding energies of around 337.0 eV and 342.3 eV are contributed to Pd 3d<sub>5/2</sub> and Pd 3d<sub>3/2</sub>, respectively. The binding energy of Pd 3d<sub>5/2</sub> in SA-Pd<sub>1</sub>/TiO<sub>2</sub> catalyst is slightly shifted to lower energy in comparison with the binding energy (337.2 eV of Pd<sup>2+</sup> 3d<sub>5/2</sub>) of the Pd<sup>2+</sup> species, indicating that the oxidation state of Pd in SA-Pd<sub>1</sub>/TiO<sub>2</sub> catalyst is near +2.

To investigate the atomic structure of SA-Pd<sub>1</sub>/TiO<sub>2</sub>, X-ray absorption fine structure (XAFS) analysis is performed. As shown in Fig. 2a, the absorption edge of SA-Pd<sub>1</sub>/TiO<sub>2</sub> located between these of PdO and Pd foil, which is slightly shifted to lower energy in comparison with PdO,

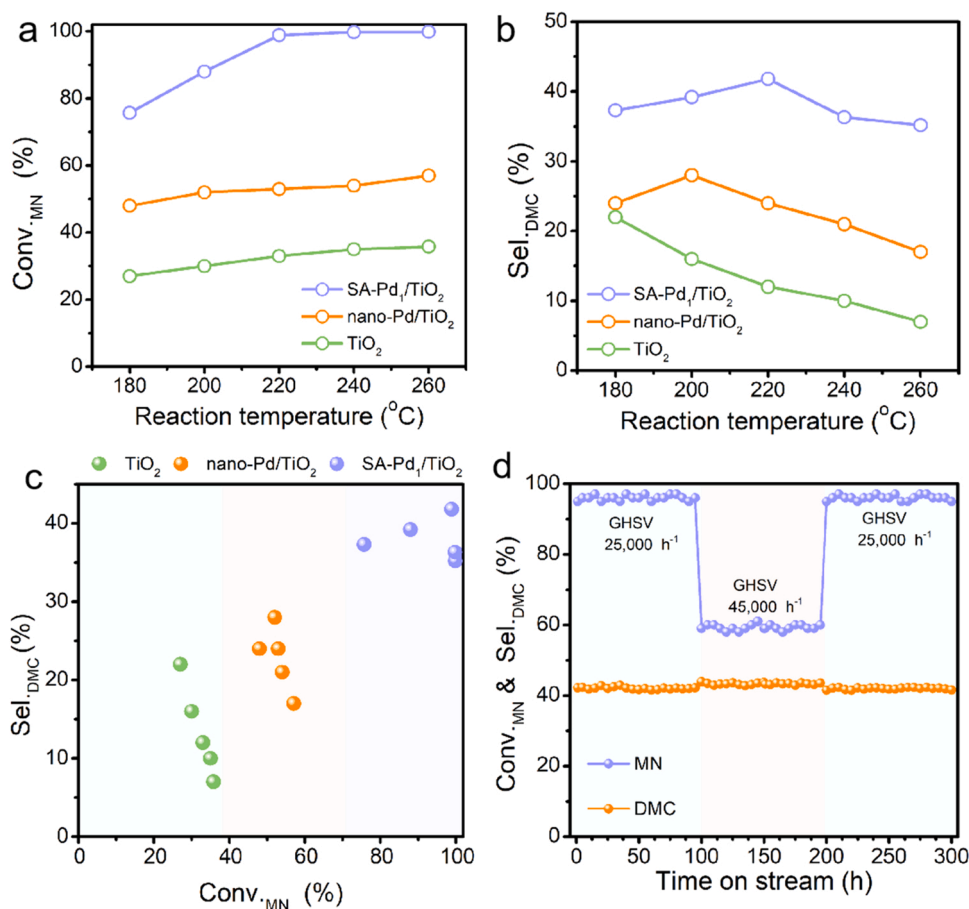


**Fig. 3.** Catalytic performance of SA-Pd<sub>1</sub>/TiO<sub>2</sub>. (a) Conversion of MN and (b) selectivity of DMC over the SA-Pd<sub>1</sub>/TiO<sub>2</sub>, nano-Pd/TiO<sub>2</sub> and TiO<sub>2</sub> catalysts. (c) Selectivity of DMC versus conversion of MN over the SA-Pd<sub>1</sub>/TiO<sub>2</sub>, nano-Pd/TiO<sub>2</sub> and TiO<sub>2</sub> catalysts. (d) MN conversion and DMC selectivity along with the time on stream over the SA-Pd<sub>1</sub>/TiO<sub>2</sub> at 220 °C with GHSV of 25,000 h<sup>-1</sup> and 45,000 h<sup>-1</sup>.

suggesting that Pd atoms in SA-Pd<sub>1</sub>/TiO<sub>2</sub> possess positive charge (near +2), which is consistent with the XPS result. And the X-ray absorption near-edge structure (XANES) curve of SA-Pd<sub>1</sub>/TiO<sub>2</sub> is similar to that of PdO, suggesting the similar first shell coordination structure from Pd-O scattering (Fig. 2a). As shown in Fig. 2b, the Fourier-transform extended X-ray absorption fine structure (FT-EXAFS) spectra of SA-Pd<sub>1</sub>/TiO<sub>2</sub> exhibits only one main peak at 1.5 Å ascribed to Pd-O interaction, similar to the peak of the first shell coordination of PdO. The peak at 2.5 Å attributed to Pd-Pd coordination that appears in Pd foils is not detected in SA-Pd<sub>1</sub>/TiO<sub>2</sub>, excluding the formation of metallic Pd-derived crystalline structure and confirming the sole existence of isolated Pd atoms.

Furthermore, wavelet transform (WT) analysis is carried out to reinforce these findings, which can discriminate the backscattering atoms and provide both radial distance resolution and k-space resolution. The WT contour plots of PdO and Pd foils demonstrate that the intensity maxima at around 5.5 Å<sup>-1</sup> and 8.5 Å<sup>-1</sup> are associated with Pd-O and Pd-Pd coordination, respectively (Fig. 2c and Fig. S5). As displayed in the WT contour plot of SA-Pd<sub>1</sub>/TiO<sub>2</sub>, only one intensity maximum at about 5.5 Å<sup>-1</sup> from Pd-O contribution is observed. And, the Pd-Pd coordination-derived intensity maximum near 8.5 Å<sup>-1</sup> is not detected. Combining AC HAADF-STEM, XAFS and WT results, the atomic dispersion of Pd in SA-Pd<sub>1</sub>/TiO<sub>2</sub> is confirmed. The quantitative least-squares EXAFS curve-fitting is performed to investigate the coordination configurations of Pd species. The best-fitting results reveal that the first shell peak at 1.5 Å originates from single Pd atoms coordinated by two O atoms (Fig. 2d and Table S1). Based on the above analysis, we performed DFT calculations to establish and optimize the structural model of SA-Pd<sub>1</sub>/TiO<sub>2</sub> (inset of Fig. 2d).

### 3.2. Catalytic performance

The as-prepared SA-Pd<sub>1</sub>/TiO<sub>2</sub> was applied in the synthesis of dimethyl carbonate (DMC) from methyl nitrite (MN) and carbon monoxide (CO) (Scheme 1). For comparison, the Pd-free TiO<sub>2</sub> and TiO<sub>2</sub> supported Pd nanoparticles catalyst (marked as nano-Pd/TiO<sub>2</sub>) were prepared (Fig. S6 to S8) and examined. The catalytic performance of SA-Pd<sub>1</sub>/TiO<sub>2</sub>, nano-Pd/TiO<sub>2</sub> and Pd-free TiO<sub>2</sub> catalysts are exhibited in Fig. S9 to S11, respectively. The MN conversion as a function of reaction temperature is shown in Fig. 3a. As the temperature rises from 180 to 220 °C, the MN conversion over SA-Pd<sub>1</sub>/TiO<sub>2</sub> increases rapidly from 75.7% to near 99.0%. In contrast, the conversion over nano-Pd/TiO<sub>2</sub> catalyst rises slowly. Even at high temperature of 220 °C, nano-Pd/TiO<sub>2</sub> merely exhibits low conversions of 53.0%. As shown in Fig. 3b, the SA-Pd<sub>1</sub>/TiO<sub>2</sub> shows higher selectivity of DMC than that of nano-Pd/TiO<sub>2</sub> during the temperature range of 180 °C to 260 °C. Compared with the SA-Pd<sub>1</sub>/TiO<sub>2</sub>, the DMC selectivity of nano-Pd/TiO<sub>2</sub> exhibits an obvious decreasing tendency with the temperature range of 200 °C to 260 °C. In addition, the MN conversion of the SA-Pd<sub>1</sub>/TiO<sub>2</sub> is 99.0% and the corresponding DMC selectivity is up to 42.0% at 220 °C, which are obviously higher than these of nano-Pd/TiO<sub>2</sub> (53.0% of MN conversion and 23.6% of DMC selectivity). Moreover, the Pd-free TiO<sub>2</sub> support shows only 32.2% of the MN conversion and near 11.7% of the DMC selectivity under the same conditions, which are much lower than those of SA-Pd<sub>1</sub>/TiO<sub>2</sub>. Notably, the space-time yield (STY) of DMC and weight-time yields (WTY) are also important indexes to evaluate the performance of catalysts and we have performed them for the SA-Pd<sub>1</sub>/TiO<sub>2</sub> and nano-Pd/TiO<sub>2</sub>. The space-time yield (STY) (4838.2 g·L<sub>cat</sub><sup>-1</sup>·h<sup>-1</sup>) and weight-

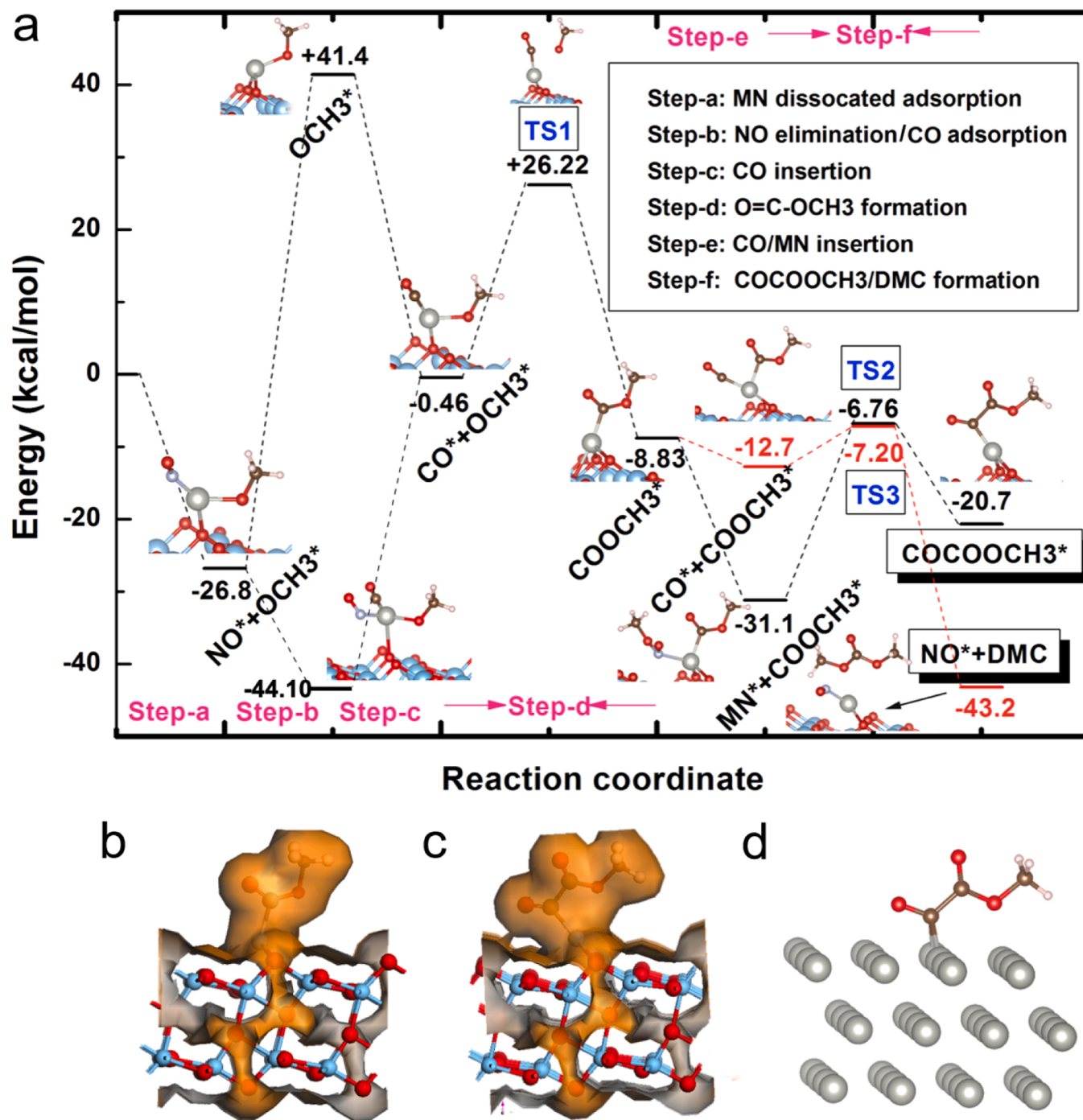


**Fig. 4.** DFT studies. (a) Reaction paths for DMC formation on SA-Pd<sub>1</sub>/TiO<sub>2</sub>. (b) The van der Waals surfaces of COOCH<sub>3</sub>-Pd<sub>1</sub>/TiO<sub>2</sub> and (c) COCOOCH<sub>3</sub>-Pd<sub>1</sub>/TiO<sub>2</sub>. (d) The optimized geometry for COCOOCH<sub>3</sub> on Pd(111) surface. Ti (cyan), O (red), Pd (silver), C (brown), N (purple) and H (pink), respectively.

time yields (WTY) (3483.5 g·kg<sub>cat</sub><sup>-1</sup>·h<sup>-1</sup>) of DMC over the SA-Pd<sub>1</sub>/TiO<sub>2</sub> are higher than these of nano-Pd/TiO<sub>2</sub> (STY: 1446.1 g·L<sub>cat</sub><sup>-1</sup>·h<sup>-1</sup>; WTY: 1041.2 g·kg<sub>cat</sub><sup>-1</sup>·h<sup>-1</sup>) and most of the previously reported Pd-based catalysts (Table S2). In addition, as shown in Fig. S12, the calculated turnover frequencies (TOF) of MN in SA-Pd<sub>1</sub>/TiO<sub>2</sub> is 7646.0 h<sup>-1</sup>, which is higher than that (2066.4 h<sup>-1</sup>) of MN in the nano-Pd/TiO<sub>2</sub>. As displayed in Fig. 3c, the majority of values of DMC selectivity versus MN conversion for SA-Pd<sub>1</sub>/TiO<sub>2</sub> are located in the upper right corner, suggesting SA-Pd<sub>1</sub>/TiO<sub>2</sub> exhibits higher MN conversion and better DMC selectivity compared with nano-Pd/TiO<sub>2</sub> and Pd-free TiO<sub>2</sub>. As shown in Fig. S9 and S10, with the increase of temperature, the selectivity toward byproduct dimethyl oxalate (DMO) over SA-Pd<sub>1</sub>/TiO<sub>2</sub> decreases more

significantly than that of nano-Pd/TiO<sub>2</sub>, which implies that single Pd atomic sites effectively inhibit the formation of byproduct DMO. The above results confirm the enhancement role of isolated Pd atoms for catalytic performance of the synthesis of DMC from MN and CO. Then, to study the effect of the valence of Pd atoms on its catalytic activity, we test the catalytic performance of SA-Pd<sub>1</sub>/TiO<sub>2</sub>-C with the calcination in air as a reference compared with SA-Pd<sub>1</sub>/TiO<sub>2</sub> with the reduction in 5% H<sub>2</sub>/Ar (Fig. S13 and S14). As shown in Fig. S13, the catalytic MN conversion and DMC selectivity of the SA-Pd<sub>1</sub>/TiO<sub>2</sub> are both higher than these of SA-Pd<sub>1</sub>/TiO<sub>2</sub>-C and nano-Pd/TiO<sub>2</sub>, indicating that the positive charge of Pd atoms in SA-Pd<sub>1</sub>/TiO<sub>2</sub> is beneficial to the activity and selectivity for this catalytic reaction.



Stability is very important consideration for practical industrial applications. Thus, we performed the long-term test of the carbonylation of MN to DMC over SA-Pd<sub>1</sub>/TiO<sub>2</sub>. We firstly assess the stability of catalyst for 100 h under the GHSV of 25000 h<sup>-1</sup>, which demonstrates the excellent activity and selectivity are maintained, always achieving above ~96% MN conversion with MN-based DMC selectivity of ~42% (Fig. 3d and Fig. S15). Then, we turn up the GHSV to 45000 h<sup>-1</sup> to evaluate the stability of catalyst under the conversion far way from 100% for another 100 h. After that, we set the GHSV back to 25000 h<sup>-1</sup> and assessed the catalyst for another 100 h. It can be seen that the SA-Pd<sub>1</sub>/TiO<sub>2</sub> catalyst still maintains the original MN conversion and DMC selectivity. The above results demonstrate that the SA-Pd<sub>1</sub>/TiO<sub>2</sub> exhibit a great stability. The SA-Pd<sub>1</sub>/TiO<sub>2</sub> after stability test is characterized, which show that the structure and isolated feature of Pd atoms in SA-Pd<sub>1</sub>/TiO<sub>2</sub> after stability test are well preserved (Figs. S16–S19).

### 3.3. Steric hindrance effect

We further performed DFT calculations to demonstrate how the SA-Pd<sub>1</sub>/TiO<sub>2</sub> catalyzed the synthesis of DMC from MN and CO and reveal why the selectivity is enhanced after downsizing nanoparticles into single-atom scale. The TiO<sub>2</sub>(101) surface structure and Pd<sub>1</sub>/TiO<sub>2</sub>(101) model was optimized and constructed (Fig. S20 and S21). As shown in Fig. 4a and Fig. S22, the reaction undergoes several steps from MN dissociated adsorption, NO elimination/CO adsorption (Fig. S23), CO insertion to COOCH<sub>3</sub> formation. The barrier of CO insertion step is 26.68 kcal/mol, and this step is exothermic by 8.37 kcal/mol. COOCH<sub>3</sub> is the one an essential intermediate in this reaction (Fig. 4b and Fig. S24). Based on it, both MN and CO can attract the isolated single Pd atoms on the TiO<sub>2</sub> substrate to form COCOOCH<sub>3</sub> and (NO\*+DMC), respectively. The formation of COCOOCH<sub>3</sub> and (NO\*+DMC) are endothermic and exothermic, and with barriers of 24.34 and 5.50 kcal/mol, respectively. Hence, in step-f, (NO\*+DMC) formation is favorable both thermodynamically and kinetically. Meanwhile, other reaction paths to generation DMO from either coupling of two COOCH<sub>3</sub> species or coupling of OCH<sub>3</sub> and COCOOCH<sub>3</sub> need to overcome higher barriers of 46.8 kcal/mol and 35.0 kcal/mol, respectively, as shown in Fig. S25 and S26.

When COCOOCH<sub>3</sub> is formed on SA-Pd<sub>1</sub>/TiO<sub>2</sub>, the active site, Pd, is almost wrapped by the O=C-C-O-C chain of the intermediate (Fig. 4c and Fig. S27), together with the TiO<sub>2</sub> substrate. Therefore, dissociating MN need to climb over a barrier of 21.1 kcal/mol to generate OCH<sub>3</sub>\* and trigger an even higher barrier (35.0 kcal/mol) DMO formation with \*COCOCH<sub>3</sub> (Fig. S26). Meanwhile, no additional active Pd site is available nearby to dissociate MN directly and to feed OCH<sub>3</sub> radical for DMO formation as it on clean Pd(111) surface (Fig. S28). In this sense, the DMO is hard to be formed based on COCOOCH<sub>3</sub>\* in SA-Pd<sub>1</sub>/TiO<sub>2</sub> model. On the contrary, the subsequent reaction to form DMO will not be halted on Pd (111) surface. The optimized configuration of COCOOCH<sub>3</sub> on Pd (111) is shown in Fig. 4d. On the metal surface, the intact Pd atoms which are close to the COCOOCH<sub>3</sub> occupied Pd site can serve as additional active sites to dissociate MN and supply new OCH<sub>3</sub> radical to initiate the DMO formation (Fig. S29–S32). The detailed reaction mechanism of CO oxidation coupling to DMO on Pd (111) surface was investigated in DFT and in situ diffuse reflectance infrared spectroscopy (DRIR). [57] For Pd (111) surface, the abundant active sites can reduce the steric hindrance effect, which is essential in SA-Pd<sub>1</sub>/TiO<sub>2</sub>. Thus, the selectivity of DMC over DMO on SA-Pd<sub>1</sub>/TiO<sub>2</sub> originates from both the steric effect of single Pd atoms on TiO<sub>2</sub> surface and the molecule volume/size of the target products.

## 4. Conclusions

In this work, we prepare highly stable SA-Pd<sub>1</sub>/TiO<sub>2</sub> catalyst for the catalytic synthesis of DMC. Moreover, we demonstrate a steric hindrance effect of single atoms induced by the unique isolation of single-

atom active sites. We believe such effect of single atoms will offer a guideline to design and optimize single-atom catalysts for their wider applications in selective catalytic reactions.

## CRedit authorship contribution statement

Shufang Ji: Methodology, Data curation, Writing – original draft. Yuanjun Chen: Data curation, Investigation, Discussion. Guofeng Zhao: Catalytic test, Data curation, Discussion. Yu Wang: XAFS data analysis. Wenming Sun: DFT Calculations, Data curation, Writing – original draft. Zedong Zhang: Data curation. Yong Lu: Review & Editing, Discussion. Dingsheng Wang: Supervision, Conceptualization, Writing – review & editing.

## Declaration of Competing Interest

The authors declare that they have no known competing financial interests or personal relationships that could have appeared to influence the work reported in this paper.

## Acknowledgements

This work was supported by Science and Technology Key Project of Guangdong Province of China (2020B010188002), the National Key R&D Program of China (2018YFA0702003), the National Natural Science Foundation of China (21890383, 21871159, 21703069), the National Postdoctoral Program for Innovative Talents (BX20180160) and the China Postdoctoral Science Foundation (2018M640113). We thank the BL14W1 station in Shanghai Synchrotron Radiation Facility (SSRF). W Sun acknowledges computational resources of "TianHe-1A" super-computer at the National Supercomputing Center in Tianjin and technical support from Tianhe Supercomputing Center of Huaihai.

## Appendix A. Supporting information

Supplementary data associated with this article can be found in the online version at doi:10.1016/j.apcatb.2021.120922.

## References

- [1] X.F. Yang, A. Wang, B. Qiao, J. Li, J. Liu, T. Zhang, Single-atom catalysts: a new frontier in heterogeneous catalysis, *Acc. Chem. Res.* 46 (2013) 1740–1748.
- [2] Y. Chen, R. Gao, S. Ji, H. Li, K. Tang, P. Jiang, H. Hu, Z. Zhang, H. Hao, Q. Qu, X. Liang, W. Chen, J. Dong, D. Wang, Y. Li, Atomic-level modulation of electronic density of metal-organic frameworks-derived Co single-atom sites to enhance oxygen reduction performance, *Angew. Chem. Int. Ed.* 60 (2021) 3212–3221.
- [3] X. Cui, W. Li, P. Ryabchuk, K. Junge, M. Beller, Bridging homogeneous and heterogeneous catalysis by heterogeneous single-metal-site, *Nat. Catal.* 1 (2018) 385.
- [4] Y. Wang, X.B. Zheng, D.S. Wang, Design concept for electrocatalysts, *Nano Res* (2021), <https://doi.org/10.1007/s12274-021-3794-0>.
- [5] L. Liu, A. Corma, Metal catalysts for heterogeneous catalysis: from single atoms to nanoclusters and nanoparticles, *Chem. Rev.* 118 (2018) 4981–5079.
- [6] A. Wang, J. Li, T. Zhang, Heterogeneous single-atom catalysis, *Nat. Rev. Chem.* 2 (2018) 65–81.
- [7] Z. Lia, X. Lua, W. Sun, L. Leng, M. Zhang, H. Li, L. Bai, D. Yuan, J.H. Horton, Q. Xu, J. Wang, One-step synthesis of single palladium atoms in WO<sub>2</sub>72 with high efficiency in chemoselective hydrodeoxygenation of vanillin, *Appl. Catal., B* 298 (2021), 120535.
- [8] M. Kou, W. Liu, Y. Wang, J. Huang, Y. Chen, Y. Zhou, Y. Chen, M. Ma, K. Lei, P. H. Xie, L. Wong, Ye, Photocatalytic CO<sub>2</sub> conversion over single-atom MoN<sub>2</sub> sites of covalent organic framework, *Appl. Catal., B* 291 (2021), 120146.
- [9] J.R. Yang, W.H. Li, D.S. Wang, Y.D. Li, Single-atom materials: Small structures determine macroproperties, *Small Struct.* 2 (2021) 2000051.
- [10] Y. Chen, S. Ji, W. Sun, Y. Lei, Q. Wang, A. Li, W. Chen, G. Zhou, Z. Zhang, Y. Wang, L. Zheng, Q. Zhang, L. Gu, X. Han, D. Wang, Y. Li, Engineering the atomic interface with single platinum atoms for enhanced photocatalytic hydrogen production, *Angew. Chem. Int. Ed.* 59 (2020) 1295–1301.
- [11] H. Song, R. Du, Y. Wang, D. Zu, R. Zhou, Y. Cai, F. Wang, Z. Li, Y. Shen, C. Li, Anchoring single atom cobalt on two-dimensional MXene for activation of peroxymonosulfate, *Appl. Catal., B* 286 (2021), 119898.
- [12] X. Guo, G. Fang, G. Li, H. Ma, H. Fan, L. Yu, C. Ma, X. Wu, D. Deng, M. Wei, D. Tan, R. Si, S. Zhang, J. Li, L. Sun, Z. Tang, X. Pan, X. Bao, Direct, nonoxidative

- conversion of methane to ethylene, aromatics, and hydrogen, *Science* 344 (2014) 616–619.
- [13] J. Zhang, Z.Y. Wang, W.X. Chen, Y. Xiong, W. Cheong, L.R. Zheng, W.S. Yan, L. Gu, C. Chen, Q. Peng, P. Hu, D.S. Wang, Y.D. Li, Tuning polarity of Cu–O bond in heterogeneous Cu catalyst to promote additive-free hydroboration of alkynes, *Chem* 6 (2020) 725–737.
  - [14] L. Lin, W. Zhou, R. Gao, S. Yao, X. Zhang, W. Xu, S. Zheng, Z. Jiang, Q. Yu, Y.W. Li, C. Shi, X.D. Wen, D. Ma, Low-temperature hydrogen production from water and methanol using Pt/ $\alpha$ -MoC catalysts, *Nature* 544 (2017) 80–83.
  - [15] Y. Xiong, W. Sun, Y. Han, P. Xin, X. Zheng, W. Yan, J. Dong, J. Zhang, D. Wang, Y. Li, Cobalt single atom site catalysts with ultrahigh metal loading for enhanced aerobic oxidation of ethylbenzene, *Nano Res* 14 (2021) 2418–2423.
  - [16] Z.H. Liu, Y. Du, P.F. Zhang, Z.C. Zhuang, D.S. Wang, Bringing catalytic order out of chaos with nitrogen-doped ordered mesoporous carbon, *Matter* 4 (2021) 3161–3194.
  - [17] S. Ji, Y. Qu, T. Wang, Y. Chen, G. Wang, X. Li, J. Dong, Q. Chen, W. Zhang, Z. Zhang, S. Liang, R. Yu, Y. Wang, D. Wang, Y. Li, Rare-earth single erbium atoms for enhanced photocatalytic CO<sub>2</sub> reduction reaction, *Angew. Chem. Int. Ed.* 59 (2020) 10651–10657.
  - [18] L. Jiao, G. Wan, R. Zhang, H. Zhou, S.H. Yu, H.L. Jiang, From metal–organic frameworks to single-atom Fe implanted N-doped porous carbons: efficient oxygen reduction in both alkaline and acidic media, *Angew. Chem. Int. Ed.* 57 (2018) 8525–8529.
  - [19] H. Jing, P. Zhu, X. Zheng, Z. Zhang, D. Wang, Y. Li, Theory-oriented screening and discovery of advanced energy transformation materials in electrocatalysis, *Adv. Powder Mater.* (2021), <https://doi.org/10.1016/j.apmat.2021.10.004>.
  - [20] S.H. Chen, B.Q. Wang, J.X. Zhu, L.Q. Wang, H.H. Ou, Z.D. Zhang, X. Liang, L. R. Zheng, L. Zhou, Y.Q. Su, D.S. Wang, Y.D. Li, Lewis acid site-promoted single-atomic Cu catalyzes electrochemical CO<sub>2</sub> methanation, *Nano Lett.* 21 (2021) 7325–7331.
  - [21] G. Liu, Y. Huang, H. Lv, H. Wang, Y. Zeng, M. Yuan, Q. Meng, C. Wang, Confining single-atom Pd on g-C<sub>3</sub>N<sub>4</sub> with carbon vacancies towards enhanced photocatalytic NO conversion, *Appl. Catal., B* 284 (2021), 119683.
  - [22] B.-H. Lee, S. Park, M. Kim, A.K. Sinha, S.C. Lee, E. Jung, W.J. Chang, K.-S. Lee, J. H. Kim, S.-P. Cho, H. Kim, K.T. Nam, T. Hyeon, Reversible and cooperative photoactivation of single-atom Cu/TiO<sub>2</sub> photocatalysts, *Nat. Mater.* 18 (2019) 620–626.
  - [23] E. Jung, H. Shin, B.-H. Lee, V. Efremov, S. Lee, H.S. Lee, J. Kim, W. Hooch Antink, S. Park, K.-S. Lee, S.-P. Cho, J.S. Yoo, Y.-E. Sung, T. Hyeon, Atomic-level tuning of Co–N–C catalyst for high-performance electrochemical H<sub>2</sub>O<sub>2</sub> production, *Nat. Mater.* 19 (2020) 436–442.
  - [24] C. Xie, Z. Niu, D. Kim, M. Li, P. Yang, Surface and interface control in nanoparticle catalysis, *Chem. Rev.* 120 (2019) 1184–1249.
  - [25] Y. Chen, S. Ji, W. Sun, W. Chen, J. Dong, J. Wen, J. Zhang, Z. Li, L. Zheng, C. Chen, Q. Peng, D. Wang, Y. Li, Discovering partially charged single-atom Pt for enhanced anti-Markovnikov alkene hydrosilylation, *J. Am. Chem. Soc.* 140 (2018) 7407–7410.
  - [26] J.R. Yang, W.H. Li, S.D. Tan, K.N. Xu, Y. Wang, D.S. Wang, Y.D. Li, The electronic metal-support interaction directing the design of single atomic site catalyst: achieving high efficiency towards hydrogen evolution, *Angew. Chem. Int. Ed.* 60 (2021) 19085–19091.
  - [27] N. Daelman, M. Capdevila-Cortada, N. López, Dynamic charge and oxidation state of Pt/CeO<sub>2</sub> single-atom catalysts, *Nat. Mater.* 18 (2019) 1215–1221.
  - [28] A.L. Han, X.J. Wang, K. Tang, Z.D. Zhang, C.L. Ye, K.J. Kong, H.B. Hu, L.R. Zheng, P. Jiang, C.X. Zhao, Q. Zhang, D.S. Wang, Y.D. Li, An adjacent atomic platinum site enables single-atom iron with high oxygen reduction reaction performance, *Angew. Chem. Int. Ed.* 60 (2021) 19262–19271.
  - [29] P. Liu, Y. Zhao, R. Qin, S. Mo, G. Chen, L. Gu, D.M. Chevrier, P. Zhang, Q. Guo, D. Zang, B. Wu, G. Fu, N. Zheng, Photochemical route for synthesizing atomically dispersed palladium catalysts, *Science* 352 (2016) 797–800.
  - [30] W.H. Li, J.R. Yang, H.Y. Jing, J. Zhang, Y. Wang, J. Li, J. Zhao, D.S. Wang, Y.D. Li, Creating high regioselectivity by electronic metal-support interaction of single-atomic-site catalyst, *J. Am. Chem. Soc.* 143 (2021) 15453–15461.
  - [31] G. Wang, R. Huang, J.W. Zhang, J.J. Mao, D.S. Wang, Y.D. Li, Synergistic modulation of the separation of photo-generated carriers via engineering of dual atomic sites for promoting photocatalytic performance, *Adv. Mater.* (2021), <https://doi.org/10.1002/adma.202105904>.
  - [32] Y. Meng, J. Li, S. Zhao, C. Shi, X. Li, L. Zhang, P. Hou, C. Liu, H. Cheng, Fluorination-assisted preparation of self-supporting single-atom Fe–N-doped single-wall carbon nanotube film as bifunctional oxygen electrode for rechargeable Zn–Air batteries, *Appl. Catal., B* 294 (2021), 120239.
  - [33] M. Zhou, S. Bao, A.J. Bard, Probing size and substrate effects on the hydrogen evolution reaction by single isolated Pt atoms, atomic clusters, and nanoparticles, *J. Am. Chem. Soc.* 141 (2019) 7327–7332.
  - [34] Q. Cao, L. Zhang, C. Zhou, J. He, A. Marcomini, J. Lu, Covalent organic framework-supported Zn single atom catalyst for highly efficient N-formylation of amines with CO<sub>2</sub> under mild conditions, *Appl. Catal., B* 294 (2021), 120238.
  - [35] S. Ji, B. Jiang, H. Hao, Y. Chen, J. Dong, Y. Mao, Z. Zhang, R. Gao, W. Chen, R. Zhang, Q. Liang, H. Li, S. Liu, Y. Wang, Q. Zhang, L. Gu, D. Duan, M. Liang, D. Wang, X. Yan, Y. Li, Matching the kinetics of natural enzymes with a single-atom iron nanozyme, *Nat. Catal.* 4 (2021) 407–417.
  - [36] L.-N. Chen, K.-P. Hou, Y.-S. Liu, Z.-Y. Qi, Q. Zheng, Y.-H. Lu, J.-Y. Chen, J.-L. Chen, C.-W. Pao, S.-B. Wang, Y.-B. Li, S.-H. Xie, F.-D. Liu, D. Prendergast, L.E. Klebanoff, V. Stavila, M.D. Allendorf, J. Guo, L.-S. Zheng, J. Su, G.A. Somorjai, Efficient hydrogen production from methanol using a single-site Pt<sub>1</sub>/CeO<sub>2</sub> catalyst, *J. Am. Chem. Soc.* 141 (2019) 17995–17999.
  - [37] D. Wang, Q. Li, C. Han, Z. Xing, X. Yang, Single-atom ruthenium based catalyst for enhanced hydrogen evolution, *Appl. Catal., B* 249 (2019) 91–97.
  - [38] A.-A.G. Shaikh, S. Sivaram, Organic carbonates, *Chem. Rev.* 96 3 (1996) 951–976.
  - [39] D. Delle Donne, F. Rivetti, U. Romano, Developments in the production and application of dimethylcarbonate, *Appl. Catal., A* 221 (2001) 241–251.
  - [40] P. Tundo, M. Selva, The chemistry of dimethyl carbonate, *Acc. Chem. Res.* 35 (2002) 706–716.
  - [41] Y. Yuan, W. Cao, W. Weng, CuCl<sub>2</sub> immobilized on amino-functionalized MCM-41 and MCM-48 and their catalytic performance toward the vapor-phase oxy-carbonylation of methanol to dimethylcarbonate, *J. Catal.* 228 (2004) 311–320.
  - [42] Y. Ono, Catalysis in the production and reactions of dimethyl carbonate, an environmentally benign building block, *Appl. Catal., A* 155 (1997) 133–166.
  - [43] B. Schäffner, F. Schäffner, S.P. Verevkin, A. Börner, Organic carbonates as solvents in synthesis and catalysis, *Chem. Rev.* 110 (2010) 4554–4581.
  - [44] P. Rounce, A. Tsolakis, P. Leung, A.P.E. York, Organic carbonates as solvents in synthesis and catalysis, *Energy Fuels* 110 (2010) 4554–4581.
  - [45] A. Arteconi, A. Mazzarini, G.J.W. Di, Nicola, Air, S. Pollution, Emissions from ethers and organic carbonate fuel additives: a review, *Water, Air, Soil Pollut.* 221 (2011) 405–423.
  - [46] K. Shukla, V.C.J.C.L. Srivastava, Alkaline Earth (Ca, Mg) and Transition (La, Y) metals promotional effects on Zn–Al catalysts during diethyl carbonate synthesis from ethyl carbamate and ethanol, *Catal. Lett.* 147 (2017) 1891–1902.
  - [47] H.-Z. Tan, Z.-Q. Wang, Z.-N. Xu, J. Sun, Y.-P. Xu, Q.-S. Chen, Y. Chen, G.-C. Guo, Review on the synthesis of dimethyl carbonate, *Catal. Today* 316 (2018) 2–12.
  - [48] R. Guo, Y. Qin, L. Qiao, J. Chen, X. Wu, Y. Yao, Enhancement of the catalytic performance in Pd–Cu/NaY catalyst for carbonylation of methyl nitrite to dimethyl carbonate: Effects of copper doping, *Catal. Commun.* 88 (2017) 94–98.
  - [49] H.-Z. Tan, Z.-Q. Wang, Z.-N. Xu, J. Sun, Z.-N. Chen, Q.-S. Chen, Y. Chen, G.-C. Guo, Active Pd (II) complexes: enhancing catalytic activity by ligand effect for carbonylation of methyl nitrite to dimethyl carbonate, *Catal. Sci. Technol.* 7 (2017) 3785–3790.
  - [50] X. Sun, Y. Li, Synthesis and characterization of ion-exchangeable titanate nanotubes, *Chem. Eur. J.* 9 (2003) 2229–2238.
  - [51] B. Xu, Z. Zhang, X. Wang, Formamide: an efficient solvent to synthesize water-soluble and sub-ten-nanometer nanocrystals, *Nanoscale* 5 (2013) 4495–4505.
  - [52] Y. Dong, S. Huang, S. Wang, Y. Zhao, J. Gong, X. Ma, Synthesis of dimethyl carbonate through vapor-phase carbonylation catalyzed by Pd-doped zeolites: interaction of Lewis acidic sites and Pd species, *ChemCatChem* 5 (2013) 2174–2177.
  - [53] H.-Z. Tan, Z.-N. Chen, Z.-N. Xu, J. Sun, Z.-Q. Wang, R. Si, W. Zhuang, G.-C. Guo, Synthesis of high-performance and high-stability Pd (II)/NaY catalyst for CO direct selective conversion to dimethyl carbonate by rational design, *ACS Catal.* 9 (2019) 3595–3603.
  - [54] S.J. Clark, M.D. Segall, C.J. Pickard, P.J. Hasnip, M.I. Probert, K. Refson, M. C. Payne, First principles methods using CASTEP, *Z. Krist. - Cryst. Mater.* 220 (2005) 567–570.
  - [55] J.P. Perdew, K. Burke, M. Ernzerhof, Generalized gradient approximation made simple, *Phys. Rev. Lett.* 77 (1996) 3865.
  - [56] N. Govind, M. Petersen, G. Fitzgerald, D. King-Smith, J. Andzelm, A generalized synchronous transit method for transition state location, *Comput. Mater. Sci.* 28 (2003) 250–258.
  - [57] Q. Li, Z. Zhou, R. Chen, B. Sun, L. Qiao, Y. Yao, K. Wu, Insights into the reaction mechanism of CO oxidative coupling to dimethyl oxalate over palladium: A combined DFT and IR study, *Phys. Chem. Chem. Phys.* 17 (2015) 9126–9134.